The "Surface Optical" Phonon in CdSe Nanocrystals

Chen Lin, David F. Kelley, Mikaela Rico, and Anne Myers Kelley*

Chemistry and Chemical Biology, University of California, Merced, 5200 North Lake Road, Merced, California 95343, United States

ABSTRACT The origin of the ubiquitous low-frequency shoulder on the longitudinal optical (LO) phonon fundamental in the Raman spectra of CdSe quantum dots is examined. This feature is usually assigned as a "surface optical" (SO) phonon, but it is only slightly affected by modifying the surface through exchanging ligands or adding a semiconductor shell. Here we present excitation profile data showing that the low-frequency shoulder loses intensity as the excitation is tuned to longer wavelengths, closer to resonance with the lowest-energy $1S_e-1S_{3/2}$ excitonic transition. Calculations of the resonance Raman spectra are carried out using a fully atomistic model with an empirical force field to calculate the phonon modes and the standard effective mass approximation envelope function model to calculate the electron and hole wave functions. When a force field of the Tersoff type is used, the calculated spectra closely resemble the experimental ones in showing mainly the higher-frequency LO phonon with $1S_e-1S_{3/2}$ resonance but showing intensity in lower-frequency features with $1P_e-1P_{3/2}$ resonance. These calculations indicate that the main LO phonon peak involves largely motion of the interior atoms, while the low-frequency shoulder is more equally distributed throughout the crystal but not surface-localized. Interestingly, very different results are obtained with the widely used Coulomb plus Lennard-Jones force field developed by Rabani, which predicts far more disordered structures and more localized phonon modes for the nanocrystals compared with the Tersoff-type potential.

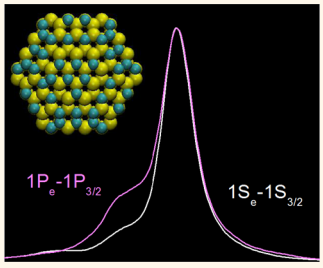

KEYWORDS: surface optical phonon · electron–phonon coupling · empirical force field · cadmium selenide · nanocrystal · quantum dot

The resonance Raman spectra of bulk CdSe and many other semiconductors are dominated by the longest-wavelength longitudinal optical (LO) phonons. While the details of the spectra depend on resonance condition, sample preparation, and polarization,[1] in CdSe, the LO phonon mode generally appears as a narrow feature at 212–213 cm^{-1}.[1,1–3] The Raman spectra of CdSe nanocrystals (NCs) show a similar feature, shifted several cm^{-1} to lower frequency from the bulk value[4–11] and attributed to the corresponding long-wavelength optical phonon of the nanocrystal. The LO phonon also appears in other spectroscopies that involve exciton–phonon coupling including single-particle and line-narrowed emission and excitation spectra[12–17] and time-domain pump–probe and photon echo experiments.[18–23]

Closer examination of Raman spectra obtained with a high signal-to-noise ratio reveals an additional, low-frequency shoulder on the LO phonon. This shoulder is seen quite consistently in nanocrystals with different sizes and shapes and with different surface chemistries[6,24–36] and also in many semiconductor materials other than CdSe. It was assigned as a "surface optical" (SO) phonon by comparison with predictions based on dielectric continuum theory for the optical phonon modes of ionic crystals.[37,38] Although alternative explanations involving only the dispersion of the LO phonons have been presented,[39] the SO assignment seems to have been widely accepted and there have been a number of efforts to correlate the frequency and/or intensity of this mode with surface properties of core–shell nanocrystals such as shell thickness and degree of alloying at the surface.[6,26,27,33,40] However, the phonon mode assignments seem tenuous given that surface modification often affects the LO phonon about as much as the "SO".[6,26–28,35] The frequencies of the surface modes of a small spherical nanocrystal are given by dielectric continuum theory as[37]

$$\Omega_{SO} = \Omega_{TO}\left[\frac{\varepsilon_0 \ell + \varepsilon_M(\ell+1)}{\varepsilon_\infty \ell + \varepsilon_M(\ell+1)}\right]^{1/2} \qquad \ell = 1, 2, 3\ldots \quad (1)$$

where Ω_{TO} is the frequency of the bulk transverse optical (TO) phonon, ε_0 and ε_∞ are the static and high-frequency dielectric

* Address correspondence to amkelley@ucmerced.edu.

Received for review February 11, 2014 and accepted March 21, 2014.

Published online March 21, 2014
10.1021/nn5008513

constants of bulk CdSe, ε_M is the static dielectric constant of the surrounding medium, and ℓ is the angular momentum quantum number. With a few exceptions,[33] the frequency of the SO mode is found to shift by far less than predicted upon replacing the organic ligands with a semiconductor shell,[6,28,29] changing the medium refractive index from about 2 to about 9. This indicates that the purely ionic, dielectric continuum model is not a good approximation for CdSe NCs.

Most Raman studies of the SO mode have been performed using a single excitation wavelength that is well to the blue of the lowest excitonic absorption peak. High-quality CdSe nanocrystals are highly fluorescent, and obtaining a Raman spectrum becomes very difficult as the excitation is tuned to longer wavelengths. (This is not a limitation for phonon spectra obtained by Fourier transformation of pump–probe time-domain data, and the band-edge excited spectra obtained in ref 18 show little or no contribution from the low-frequency shoulder.) However, many different transitions contribute to the absorbance of CdSe nanocrystals at shorter excitation wavelengths,[41] and the modes contributing to different parts of the optical phonon band may have different degrees of resonance enhancement from different excitonic transitions. In our previous excitation profile study on CdSe nanocrystals,[11] we focused on the integrated intensity of the sharp peak plus its shoulder, but we did note that the "LO phonon" band became narrower at longer excitation wavelengths approaching the lowest-energy excitonic transition. In this work, we carefully examine the excitation wavelength dependence of the relative intensities of the sharp, higher-frequency peak and the broader, lower-frequency shoulder for spherical CdSe nanocrystals with different surface treatments. We then compare these to Raman spectra calculated on resonance with different electron–hole states using phonon modes generated from two different empirical potentials for CdSe: the widely used Coulomb plus Lennard-Jones force field of Rabani,[42] and a modification of the covalent Tersoff-type potential developed by Benkabou *et al.*[43]

EXPERIMENTAL RESULTS

Resonance Raman excitation profile measurements were carried out on four different samples: CdSe synthesized through the standard method (expected Se-rich surface) without fluorescence quenching, a similar sample with fluorescence quenching by ligand exchange with hexadecanethiol, CdSe with a Cd-rich surface and hexadecanethiol quenching, and CdSe/ZnSe core–shell with hexadecanethiol quenching. The normalized absorption spectra of the four samples are shown in Figure 1.

Although extensive curve fitting was carried out on all data, the results are most clearly conveyed by simply

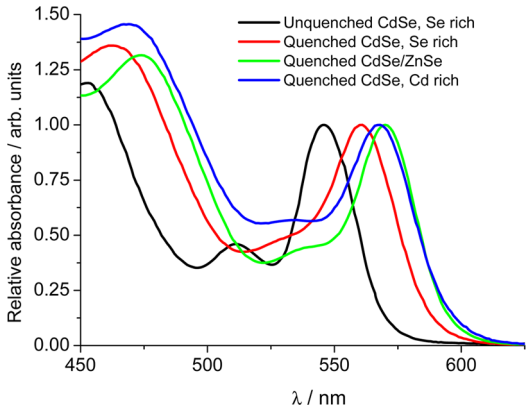

Figure 1. Optical absorption spectra of the four CdSe nanocrystal samples.

examining plots of the normalized optical phonon region of each sample as a function of excitation wavelength (Figure 2). In all four samples examined, the optical phonon spectra show a moderately strong low-frequency shoulder (SO band) when excited at short wavelengths, then undergo a fairly sudden narrowing (reduction in the intensity of the shoulder) at excitation wavelengths longer than a certain value. For the unquenched Se-rich sample (absorption maximum 546 nm), the narrowing occurs between 476.5 and 488.0 nm (2671 to 2177 cm^{-1} above the λ_{max}). For the quenched sample (absorption max 561 nm), it occurs between 496.5 and 514.5 nm (2316 to 1611 cm^{-1} above the λ_{max}). For the Cd-rich sample (absorption max 568 nm), the narrowing occurs between 514.5 and 532.0 nm (1830 to 1191 cm^{-1} above the λ_{max}). For the core–shell nanocrystals (absorption max 570 nm), it occurs between 514.5 and 532 nm (1892 to 1253 cm^{-1} above the λ_{max}). Although the instrumental resolution narrows slightly from 458 to 532 nm excitation, this does not account for the sudden narrowing of the Raman spectra of different samples at different excitation wavelengths.

These observations strongly suggest that the phonon mode(s) making up the low-frequency shoulder are relatively insensitive to the nature of the NC surface and obtain relatively greater resonance enhancement from higher-lying excitonic states (*e.g.*, $1P_e$–$1P_{3/2}$) than do the mode(s) making up the higher-frequency LO phonon. To understand the origins of these effects, we turn to analysis of the calculated phonon modes and resonance Raman spectra.

COMPUTATIONAL RESULTS

Comparison of Force Fields. The Rabani force field contains solely two-body terms and includes long-range Coulombic interactions, while the Tersoff force field includes three-body terms but has no long-range interactions. Despite these large differences, both force fields do a reasonably good job of reproducing many of the physical properties of bulk CdSe. The

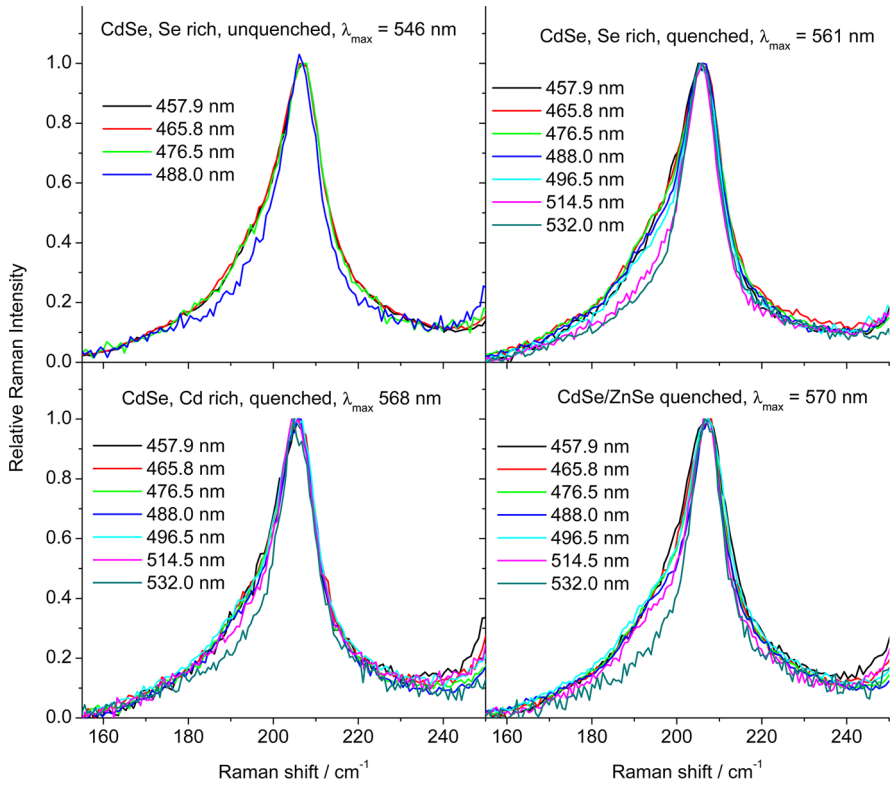

Figure 2. Normalized resonance Raman spectra of the four CdSe samples in the optical phonon region. The rising intensity at the high-frequency side of the plots is from the tail of the chloroform solvent peak at 261 cm^{-1}.

Rabani potential gives lattice constants of a = 4.38 Å and c = 6.96 Å, while the Tersoff potential gives a = 4.35 Å and c = 7.10 Å (experimental values, a = 4.34 Å and c = 7.02 Å).[42] The bulk modulus calculated from the Rabani potential is 45 GPa, while the Tersoff potential gives 48 GPa (experimental value 53 GPa).[42] The Rabani potential gives frequencies of 219 and 205 cm^{-1} for the highest-frequency LO phonon at the Γ point and at k = 0.5 along the A direction, respectively, while the Tersoff potential gives 213 and 211 cm^{-1}; the experimental values taken from Figure 1 of ref 44 appear to be about 207 and 199 cm^{-1}. All in all, crystallographic and LO frequency results for the bulk material at 1 atm give little reason to prefer one potential over the other.

The two potentials do, however, make very different predictions for the TO phonon frequencies. The highest frequency TO phonon is calculated at 153 cm^{-1} with the Rabani potential, giving an LO/TO frequency ratio of 1.43. In contrast, the Tersoff potential gives degenerate LO and TO modes, so LO/TO = 1.00. The experimental result from inelastic neutron scattering[44] is LO/TO = 1.19. This value is consistent with the Lyddane–Sachs–Teller (LST) relation,[45] $\varepsilon_0/\varepsilon_\infty = \omega_{LO}^2/\omega_{TO}^2$, where ε_0 (9.3) and ε_∞ (6.25) are the static and high-frequency dielectric constants, respectively.[46] The LST relation gives LO/TO = 1.22. This analysis indicates that the Rabani potential overestimates the Coulombic contribution to the potential. The Tersoff potential is the other extreme—it has no Coulombic contribution to the potential.

Because Coulombic interactions are much longer-ranged, the Rabani potential gives a much larger change in geometry between the bulk crystal and the nanocrystal than does the Tersoff potential. This is manifested most obviously in the energy minimizations, where the change in energy between bulk crystal atomic positions and equilibrium positions for a 3.2 nm diameter spherical crystal is more than 100 eV with the Rabani potential and only about 2 eV with the Tersoff potential. The final, optimized structures deviate much more from the bulk crystal geometry with the Rabani potential and are also considerably more disordered. This can be seen most clearly by simply looking at the positions of the atoms along the z axis (the c direction of the crystal), shown in Figure 3 for one representative structure. The high degree of disorder in the Rabani structure is hard to reconcile with the observation of clean atomic planes in high-resolution TEM images of high-quality CdSe nanocrystals.[47] (Note that these are zero-temperature calculations and greater disorder would be observed at room temperature.) On the basis of these considerations, we conclude that the Tersoff potential better describes the bonding in CdSe quantum dots. We note that the different amounts of disorder also manifest themselves in the form of the calculated phonon modes. In a perfect bulk crystal at 0 K, all of the phonon modes are completely delocalized

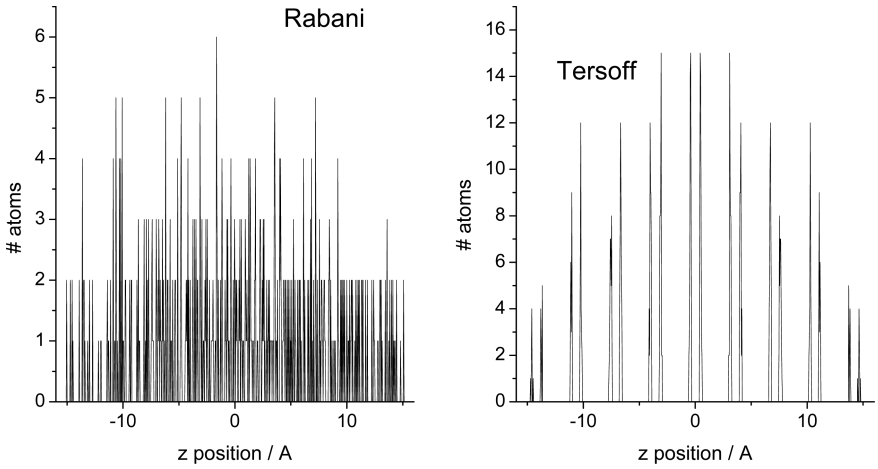

Figure 3. Histogram of atomic positions along the *z* axis for one representative structure following energy minimization with either the Rabani (left) or Tersoff (right) potential.

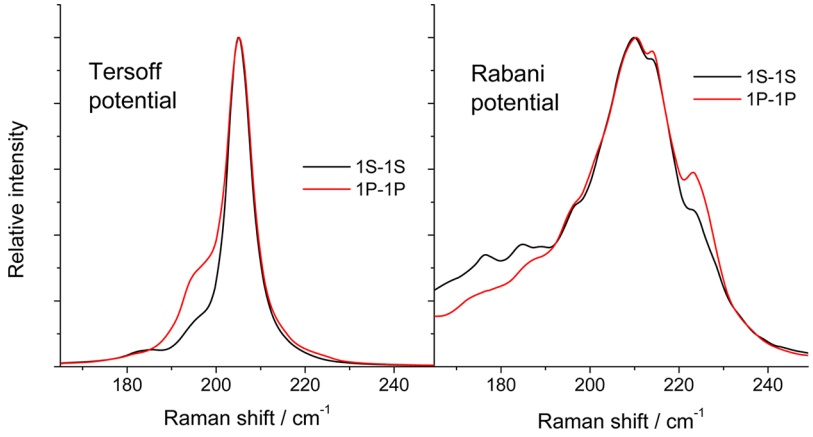

Figure 4. Resonance Raman spectra calculated for an ensemble of ~3.2 nm diameter CdSe NCs using the Tersoff potential (left) and the Rabani potential (right), on resonance with either the $1S_e-1S_{3/2}$ transition (black) or the *z*-component of the $1P_e-1P_{3/2}$ transition (red).

throughout the crystal. The Tersoff-optimized nanocrystals similarly have most of their calculated phonon modes delocalized throughout the crystal; however, in the Rabani-optimized NCs, many of the phonons are mostly localized to just a small group of a dozen or so atoms because of the disorder-induced symmetry breaking.

Calculated Raman Spectra. Figure 4 shows Raman spectra calculated on resonance with the $1S_e-1S_{3/2}$ and with the $1P_e-1P_{3/2}$ (z-component) transitions for both the Tersoff and Rabani potentials. These spectra are each averages of 12 slightly different structures. The Tersoff potential gives a sharp LO phonon peak with two very weak low-frequency shoulders for 1S-resonant excitation, while 1P-resonant excitation shows the same sharp LO peak plus a considerably stronger low-frequency shoulder. The frequency separation between peak and shoulder (about 11 cm^{-1}) and the relative intensities of the two features in the 1P-resonant spectrum are in reasonably good agreement with the experimental data of Figure 2. The ensemble-averaged spectra calculated from the Rabani potential, in contrast, are much broader and show both a very extended low-frequency shoulder and a couple of weak high-frequency shoulders. Neither the 1S-resonant nor the 1P-resonant spectra are very similar to the experimental data. For the remainder of the analysis, we focus on spectra calculated with the Tersoff potential.

Figure 5 compares the spectra calculated on resonance with four different excitonic states: $1S_e-1S_{3/2}$, both *z*- and *x*-components of the $1P_e-1P_{3/2}$, and $1S_e-2S_{3/2}$. The two P-type excitations give very similar spectra that closely resemble the experimental ones, while the $1S_e-2S_{3/2}$ and $1S_e-1S_{3/2}$ resonant spectra are nearly identical. The P−P resonant spectra appear to consist of a sharp, strong high-frequency line and a broader, weaker low-frequency shoulder, but in fact, both features have contributions from a number of different phonon modes. Figure 6 shows calculated spectra for both $1S_e-1S_{3/2}$ and $1P_e-1P_{3/2}$ resonance for two different individual structures and then the decomposition of those spectra into contributions from individual normal modes. When each frequency

is assigned a 4 cm^{-1} Lorentzian line width, the underlying modes become unresolved. Each of the 12 structures shows both the sharper peak and the low-frequency shoulder, but different structures do give slightly different frequencies and relative intensities for the two components, and ensemble averaging produces the somewhat less resolved spectra shown in Figure 5.

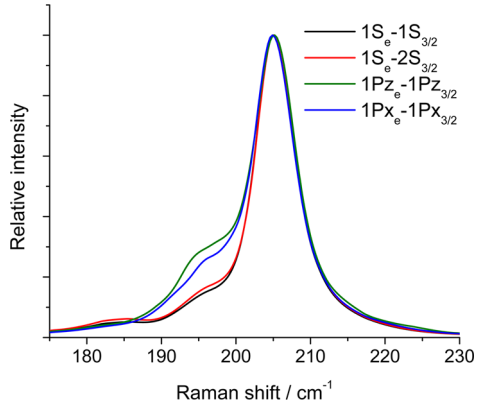

Figure 5. Resonance Raman spectra calculated for an ensemble of ~3.2 nm diameter CdSe NCs using the Tersoff potential and assuming resonance with the four different excitonic transitions indicated.

In order to address the characterization of the low-frequency shoulder as a "surface" mode, the following quantity was calculated for each phonon mode of each of the 12 structures:

$$R_i = \frac{1}{r_{avg}} \frac{\sum_j D_i(j) r(j)}{\sum_j D_i(j)} \quad (2)$$

where $r(j)$ is the radial distance of atom j from the origin, $D_i(j)$ is the absolute displacement of atom j in normal mode i, and $r_{avg} = (\sum_j r(j))/N_{atom}$ is the average radial distance from the origin. With this definition, $R_i = 1$ if the displacements are, on average, distributed

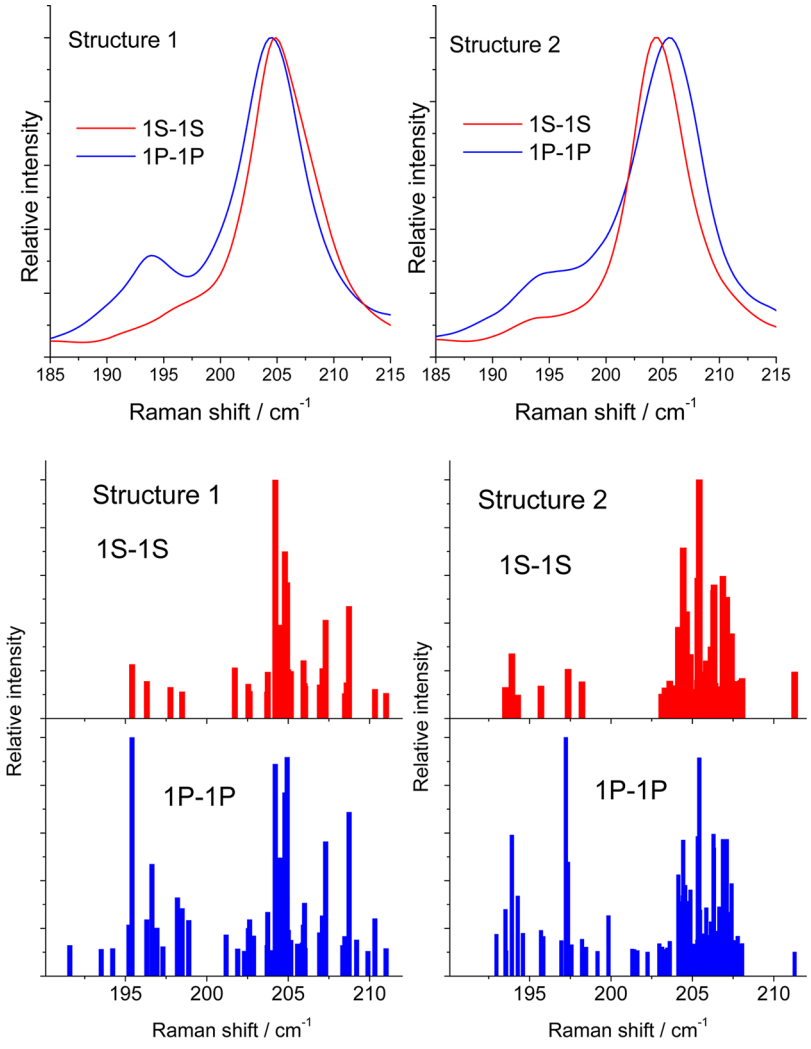

Figure 6. Top: calculated resonance Raman spectra (Tersoff potential) for two separate nanocrystal structures with both $1S_e-1S_{3/2}$ and $1P_e-1P_{3/2}$ resonance. Bottom: individual phonon modes that make up each spectrum. The height of each bar is proportional to its calculated Raman intensity, and all modes having at least 10% the intensity of the strongest line are plotted.

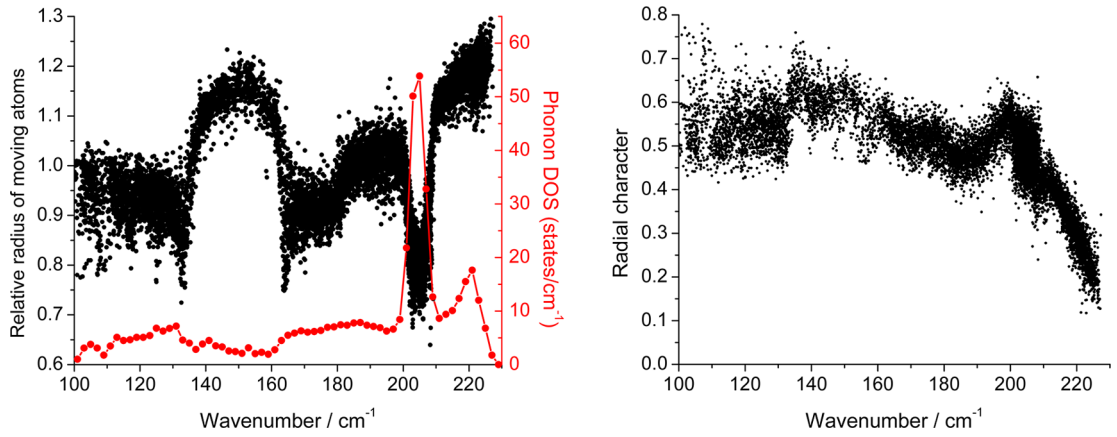

Figure 7. Quantity R_i (eq 2) and density of states *versus* mode frequency for all of the phonon modes in the 100−230 cm^{-1} range for all 12 structures (left panel) and the radial character of each of the modes (eq 3, right panel).

equally among atoms independent of their distance from the origin. A "surface mode" should have $R_i > 1$, while a mode localized to the interior of the NC has $R_i < 1$. In the continuum limit, the summation in eq 2 can be replaced by an integral and a mode localized at the surface gives $R_i = 4/3$. Figure 7 shows a scatter plot of the correlation between this quantity and the frequency of the mode for 3.2 nm NCs. The phonon modes making up the LO phonon, near 205 cm^{-1}, have a large density of states and are mostly localized to the interior of the NC. The modes assigned to the SO phonon at 185−200 cm^{-1} have a relative radial value that is close to 1.0 and are therefore neither surface- nor interior-localized. Interestingly, the modes in the 140−160 cm^{-1} region and above 210 cm^{-1} do involve preferential motion of the surface atoms, but these modes are not calculated to have significant Franck−Condon activity nor are they observed in the experimental resonance Raman spectra.

Although the lower-frequency modes have a small density of states, there is considerable density of states for the modes above 210 cm^{-1}. Although calculated to have very small electron−phonon couplings and therefore not observed in the Raman spectrum, these modes have R_i values of about 1.2, approaching the surface limiting value of 4/3. These are calculated modes that one could reasonably describe as being surface phonons. To further describe the atomic motions associated with all of the phonon modes, we have calculated the extent to which these motions are radial or tangential to the particle surface. Specifically, for each mode we calculate

$$C_i = \sum_j |\hat{v}_{j,i} \cdot \hat{r}_j| \left(\frac{|\vec{v}_{j,i}|}{\sum_j |\vec{v}_{j,i}|} \right) \quad (3)$$

where $\vec{v}_{j,i}$ is the displacement of atom j in mode i, $\hat{v}_{j,i}$ is the unit vector along the direction of the displacement of atom j in mode i, and $\hat{r}_j$ is the unit vector along the radius of atom j. The quantity in parentheses weights each dot product by the relative contribution of that atom's motion to the normal mode. If all of the dot products are zero (pure tangential motion), $C_i = 0$. If all of the dot products are 1 or −1 (pure radial motion), then $C_i = 1$. The scatter plot of these radial components is also shown in Figure 7. The LO phonons result in atomic motions that are, on average, isotropic—the radial character is very close to 0.50. In contrast, the high-frequency surface modes have a small radial component, as low as 0.20. This indicates that in these modes the atoms move primarily parallel to the surface.

DISCUSSION

Although there have been a number of large-scale atomistic simulations of phonon modes in other types of semiconductor nanocrystals,[48−53] nearly all discussions of phonons in CdSe nanocrystals have referred to dielectric continuum models such as described in refs 37 and 38. Fonoberov and Balandin[38] show plots of the phonon potentials of representative modes for spherical wurtzite NCs that are helpful in visualizing both the "confined" and the "interface" (surface) modes obtained from this treatment. Both types of modes have well-defined angular momenta (ℓ and m) as expected for a spherically symmetric structure. Real nanocrystals, however, are composed of a finite number of discrete atoms and cannot be perfectly spherical, and while we have tried to construct our model NCs to be as nearly spherical as possible, the resulting phonon modes do not have well-defined angular momenta. We have calculated the projection of the angular dependence of the atomic displacements onto each spherical harmonic up to $\ell = 4$, and we find that the largest projection has an absolute magnitude of no more than 0.5, and much smaller for most modes. That is, most of the phonon modes have an angular dependence that is a superposition of many different Y_ℓ^m, with no single one being dominant. Thus, there does not

appear to be any clear mapping of the phonon modes predicted by dielectric continuum theory onto those obtained from our atomistic simulations for NCs having ~600 atoms.

Neither the experimental results (ours and those of other workers) nor our calculations give much support for characterizing the Raman shoulder at 185–200 cm^{-1} as a surface mode. Rather, this shoulder appears to originate from a collection of optical phonons having nodal patterns that are preferentially enhanced by resonance with the $1P_e-1P_{3/2}$ and/or other transitions that occur in the wavelength region where most Raman spectra are excited, considerably above the first $1S_e-1S_{3/2}$ excitonic absorption peak. The fact that all of our samples show a strong reduction of intensity in the low-frequency shoulder as the excitation wavelength is tuned to longer wavelengths, independent of surface chemistry or the presence of a semiconductor shell, strongly suggests that the shoulder is not specifically associated with the surface but rather reflects the spatial distribution of the electron–hole wave functions with which the Raman excitation is resonant.

In bulk CdSe, the highest-frequency phonon is the LO phonon at the Γ point. The LO phonons with larger wavevectors, that is, more nodes in the phonon wave function, have slightly lower frequencies. The 1S electron and hole wave functions also have no nodes and are largely confined to the interior of the nanocrystal, and we calculate that $1S_e-1S_{3/2}$ resonant excitation enhances primarily the NC phonons whose frequencies are similar to that of the bulk $k = 0$ mode and, as indicated in Figure 7, involve mainly motions of the interior atoms. The 1P electron and hole functions have an angular node and have more charge density near the surface of the NC, and excitation on resonance with the $1P_e-1P_{3/2}$ exciton enhances both the high-frequency, bulk-like phonons (the "LO" phonon) and a collection of slightly lower-frequency modes that are less localized to the NC interior and presumably have more nodes in their wave functions (the SO phonon). When valence-band mixing is included, both the $1S_{3/2}$ and the $2S_{3/2}$ hole functions have no nodes (when summed over all four M components), and although they have rather different radial distributions, both generate nearly the same resonance Raman spectrum (Figure 5). In contrast, the *n*S hole functions calculated without S–D mixing have $(n - 1)$ radial nodes, and the calculated $1S_e-2S_{3/2}$ and $1S_e-3S_{3/2}$ resonant Raman spectra using these pure *n*S functions are dominated by the low-frequency SO band. These observations can be generalized to conclude that the more nodes the electron and/or hole wave functions contain, the more lower-frequency optical phonons will be resonantly enhanced. We note that valence-band mixing has a large effect on the 2S hole function but only a small effect on the 1S; the $1S_e-1S_{3/2}$ resonant Raman spectrum calculated using pure 1S envelope functions differs only slightly from that calculated from the S–D mixed functions. Similarly, we find that adding small amounts of 1F radial function to the 1P hole function changes the wave function only slightly and slightly increases the intensity in the low-frequency shoulder.

A full understanding of why the modes in the 185–200 cm^{-1} range gain intensity with shorter-wavelength excitation is hampered by the complexity of the absorption spectrum in this region. Norris and Bawendi[41] identified at least five transitions within the first ~4000 cm^{-1} above the $1S_e-1S_{3/2}$ absorption, tentatively assigned as $1S_e-2S_{3/2}$, $1S_e-1S_{1/2}$, $1P_e-1P_{3/2}$, $1S_e-2S_{1/2}$, and $1P_e-1P_{5/2}/1P_e-1P_{1/2}$, along with an unassigned underlying continuum absorption. Our previous excitation profile study[11] required inclusion of four transitions above the $1S_e-1S_{3/2}$, not counting the fine-structure splitting. While the transitions that involve no change in principal quantum number (1S–1S and 1P–1P) are expected to carry most of the absorption oscillator strength, the contribution of each state to the resonance Raman spectrum also depends on other factors, chiefly the Huang–Rhys factors and the electronic dephasing rates. However, independent of the exact composition of the absorption spectrum, higher-energy excitations will generally involve electron and/or hole wave functions that have more nodes, and these more structured excitonic wave functions couple more strongly to the lower-frequency components of the optical phonon band.

Figure 7 indicates that the modes in the 185–200 cm^{-1} range are not particularly surface-localized. This figure, however, could be misleading in that it shows all of the calculated modes, many of which have little or no Raman intensity. Another way to gauge the contribution of motions of surface atoms to the Raman spectrum is shown in Figure 8. Here we compare the $1P_z-1P_z$ resonant spectrum calculated in the usual way (equivalent to the red curves in Figure 4, left, and Figure 5) with the same spectrum calculated under the artificial assumption that the electron and hole wave functions are confined to a radius that is 75% of the true radius. In this way, motions of the surface atoms contribute negligibly to the Raman intensities. Removing the surface atom contributions reduces the intensity of the low-frequency shoulder with P-resonant excitation but does not eliminate it. In contrast, the higher-frequency, sharper feature is hardly affected by removing surface atom contributions.

The calculated resonance Raman spectra are not expected to agree quantitatively with experiment because of a variety of approximations that have been employed. As mentioned above, there is an inconsistency in considering the Raman enhancement to arise purely from the changes in the interatomic Coulombic forces upon electron–hole pair creation when the

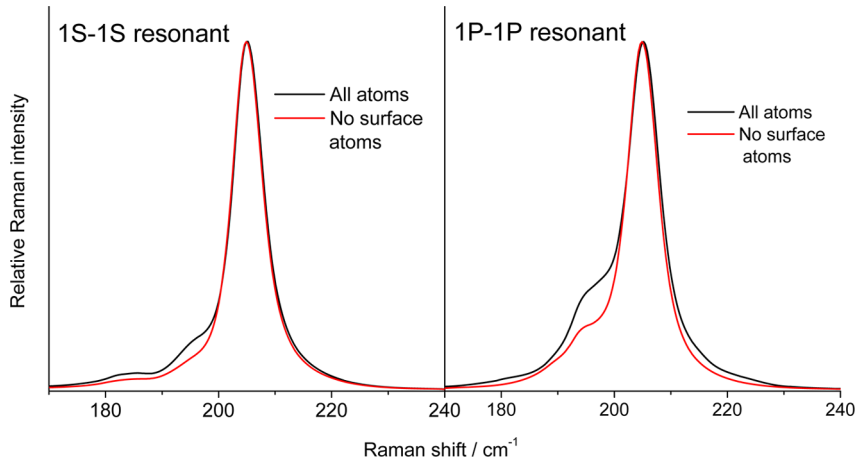

Figure 8. Raman line shapes (Tersoff potential) for 1S−1S and $1P_z$−$1P_z$ resonant excitation calculated in the usual way (black curves) and calculated assuming that the electron and hole wave functions are confined to 75% of the full NC radius (red curves).

ground-state force field does not include explicit Coulombic interactions. The assumption that the resonance Raman intensities are proportional to $\Delta^2\omega^2$ is valid only for certain ranges of resonance conditions and electronic dephasing times. In real systems, resonance with a single excitonic transition as implied in Figure 5 can rarely be achieved. Multiple excitonic transitions will usually contribute to the enhancement, with weights that depend on a variety of photophysical parameters and experimental conditions, and the contributions from the different resonant states must be added at the amplitude level before squaring to get the observed Raman intensity, resulting in interference effects among excitonic transitions.[11] Along similar lines, the contributions from each of the angular momentum fine-structure components of each exciton should also be included separately in calculating the resonance Raman amplitude. We have chosen to keep this analysis as simple as possible in order to avoid having to choose values for a large number of poorly determined additional parameters. We believe that the qualitative conclusions reached through this simple analysis are valid, but quantitative agreement with experiment would require much more detailed calculations on specific systems similar to those presented in ref 11.

The above data and analyses give a self-consistent picture to explain the optical phonon Raman line shapes in CdSe NCs based on an effective mass envelope function model for the electron and hole wave functions and an empirical interatomic potential to obtain the structures and phonon modes. An important caveat is that the success of this approach depends critically on the type of interatomic potential employed. The widely used Coulomb plus Lennard-Jones potential of Rabani does not predict Raman line shapes that closely resemble the experimental ones for any choice of excitonic resonance, as shown in Figure 4. The large amount of disorder present in NC structures minimized with GULP and the Rabani potential (*e.g.*, Figure 3) appears inconsistent with the observation of well-defined atomic planes in HRTEM images as well as sharp X-ray diffraction peaks from high-quality nanocrystals. The Tersoff potential contains no explicit charges on the atoms, and while the parameters of that potential can mimic the Coulombic contribution to the short-range interactions, there should also be long-range Coulombic forces that are not captured by this potential. It should also be noted that our calculations are carried out on bare NCs without ligands or solvent. Inclusion of a dielectric medium surrounding the NC will reduce the long-range Coulombic interactions and might produce better structures with the Rabani potential.

CONCLUSIONS

The primary conclusion of this study is that the sharp "LO phonon" at 205−208 cm^{-1} and the shoulder at 185−200 cm^{-1} both represent a superposition of contributions from a number of different phonon modes of the CdSe nanocrystal. The modes contributing to the sharp peak mostly involve motions of the atoms in the interior of the NC, while the modes contributing to the low-frequency shoulder involve atomic motions more equally distributed throughout the NC but are not well-described as surface phonons. Resonance with the lowest-energy $1S_e$−$1S_{3/2}$ excitonic transition preferentially enhances the higher-frequency interior-localized modes, which have the greatest spatial overlap with the nodeless, interior-localized 1S electron and hole wave functions. Resonance with higher-energy excitonic transitions such as the $1P_e$−$1P_{3/2}$ provides more enhancement of the lower-frequency components. Apparent correlations between alloying at the core−shell interface and the frequency or intensity of the low-frequency shoulder

should be interpreted with care because they may reflect mostly changes in the extent of resonance with different excitonic transitions as the absorption spectra shift relative to a fixed Raman excitation wavelength.

EXPERIMENTAL METHODS

Synthesis of Semiconductor Nanocrystals. The procedures for sample preparation were similar to those described in refs 54 and 55. In a typical CdSe (Se-rich) synthesis, cadmium oxide (CdO, 26 mg), oleic acid (OA, 0.4 mL), and octadecene (ODE, 3 mL) were added into a 25 mL three-neck flask, purged with nitrogen, and heated to ~250 °C until the solution was clear. This Cd precursor solution was then cooled to room temperature, and 1 g of octadecylamine (ODA) and 0.4 g trioctylphosphine oxide (TOPO) were added. It was again purged with nitrogen and reheated to 280 °C for the injection of the Se precursor (78 mg of Se, 1 mL of ODE, and 0.6 mL of trioctylphosphine (TOP)). The temperature after injection dropped to about 252 °C, and the reaction continued for about 1 min before being stopped. The resulting CdSe nanocrystal solution was then extracted by hexane/methanol (1:1 v/v) two times, and the organic layer was separated and heated to 75 °C to remove the residual hexane and methanol for Raman measurement or further treatment. Growth at an initial nucleation temperature of 280 °C is known to yield the wurtzite crystal structure exclusively; the zinc blende structure requires nucleation at a much lower temperature.[56−59]

For the growth of the ZnSe shell, 1 mL of Zn solution (0.2 M, with 162.74 mg of ZnO, 2.52 mL of OA, 7.5 mL of ODE) and 0.5 mL of Se precursor solution (0.2 M) were added dropwise into the purified CdSe core solution (~10^{-7} mol CdSe in ~3 mL of ODE) at 235 °C, and the total shell growth time was about 7 min. For the synthesis of Cd-rich CdSe, instead of using Zn and Se precursors as for ZnSe shell growth, ~0.95 mL of Cd precursor (0.1 M) was added dropwise to the CdSe solution at 185 °C. The total reaction time was ~9 min. Fluorescence of samples was quenched by mixing 0.2 mL hexadecanethiol and 2 mL of toluene with 1 mL of purified QD solution. The mixture was stirred at 82−100 °C for ~2 h under nitrogen until the ligand exchange was complete.

Raman Spectroscopy. The Raman measurements, including depolarization ratios, were carried out as described in ref 11. All samples were dissolved in chloroform at optical densities ranging from ~0.38 to ~0.78/mm. These are higher concentrations than used in ref 11 because we wished to minimize interference from solvent peaks and were not concerned with obtaining accurate absolute scattering cross sections. The laser power at the sample was around 0.5 mW. All measurements were performed on samples that were continuously translated to prevent local heating or accumulation of photoproducts. Signal was integrated on the detector for 60−120 s before being read out, and 5−30 such integrations (10−30 min total) were summed to obtain the spectrum of each sample. At the fixed physical slit width employed, the spectral resolution was about 8−11 cm^{-1} over the range of excitation wavelengths from 532 to 458 nm.

Computational Methods. Two different empirical interatomic potentials were employed. Nearly all prior molecular dynamics calculations on bulk or nanosized CdSe have employed the Rabani two-body potential,[42] which consists of a Lennard-Jones term plus a Coulomb term:

$$V_{\text{Rabani}} = \sum_i \sum_{j>i} \frac{q_i q_j}{r_{ij}} + 4\varepsilon_{ij}\left\{\left(\frac{\sigma_{ij}}{r_{ij}}\right)^{12} - \left(\frac{\sigma_{ij}}{r_{ij}}\right)^{6}\right\} \quad (4)$$

The sums in eq 4 run over all pairs of atoms. The parameters of the potential were taken directly from ref 42 and are given in Table 1. This potential assumes that the bonding is mostly ionic; the Coulombic interactions are dominant, and there is no dependence on bond angles.

Although the Rabani potential is widely used, our initial results indicated an apparently unphysical amount of structural reorganization in small nanocrystals compared with the bulk. Therefore, we also tried a potential of the Tersoff form, which is generally used for crystals in which the bonding is largely covalent. This potential contains no explicit Coulombic interactions but has both two-body and three-body terms:

$$V_{\text{Tersoff}} = \sum_i \sum_{j>i} f_c(r_{ij})[A\exp(-\lambda_1 r_{ij}) - Bb_{ij}\exp(-\lambda_2 r_{ij})] \quad (5)$$

where

$$f_c(r_{ij}) = \begin{cases} 1, & r < R - D \\ \frac{1}{2} - \frac{1}{2}\sin\left[\frac{\pi}{2}\frac{(r-R)}{D}\right], & R - D < r < R + D \\ 0, & r > R + D \end{cases} \quad (6)$$

and

$$b_{ij} = (1 + \beta^n \xi_{ij}^{n_1})^{-1/(2n)} \quad (7)$$

$$\xi_{ij} = \sum_{k \neq i,j} f_c(r_{ij}) g(\theta_{ijk}) \quad (8)$$

$$g(\theta) = 1 + \frac{c^2}{d^2} - \frac{c^2}{d^2 + (h - \cos\theta)^2} \quad (9)$$

The parameters of this potential were slightly adjusted from those originally given by Benkabou[43] to better reproduce the lattice constants, phonon frequencies, and bulk modulus of bulk CdSe. The final parameters employed are given in Table 2.

Model nanocrystals were constructed as follows. The atomic coordinates of a bulk lattice were first generated using the lattice constants that result from a bulk calculation using the desired potential (Rabani or Tersoff). An origin for the NC was then selected, either at the center of a unit cell or not. A radius was chosen, and all atoms outside that radius were eliminated. Any atoms having fewer than two nearest neighbors (defined as atoms of the opposite type within a distance of 2.9 Å) were sequentially eliminated from the structure. This resulted in nearly spherical crystals that were in some cases stoichiometric

TABLE 1. Parameters of the Rabani Potential (eq 4)[a]

parameter	q	σ/Å	ε/meV
Cd	1.18	1.98	1.4477
Se	−1.18	5.24	1.2840

[a] Combining rules: $\varepsilon_{ij} = (\varepsilon_i \varepsilon_j)^{1/2}$ and $\sigma_{ij} = (\sigma_i + \sigma_j)/2$.

TABLE 2. Parameters of the Tersoff Potential (eqs 5−9)

parameter	value
A/eV	5214
B/eV	239.5
λ_1/Å^{-1}	3.1299
λ_2/Å^{-1}	1.7322
β	1.5724×10^{-6}
n	0.78734
c	100390
d	16.217
h	−0.57058
R/Å	3.175
D/Å	0.15

and in other cases had a small excess of Cd or Se (no more than 6 "extra" atoms out of ~600 total) depending on the choice of origin and radius. These structures were then used as input for a calculation of the phonon eigenmodes and frequencies *via* the general utility lattice program (GULP)[60] following energy minimization. In principle, this should produce all real phonon frequencies, but in practice, there were often a few small (few cm^{-1}) imaginary frequencies because of imperfect energy minimization. For each type of calculation, 12 slightly different structures were generated by varying the origin and radius by small amounts (≤10% and less than a bond length, respectively), and the spectra of the 12 were averaged to give the reported spectra. A single potential function was assumed for all atoms of a given type, whether surface or interior. All calculations were carried out at zero temperature.

In order to calculate the Raman spectrum for each structure, electron and hole wave functions were calculated using the particle-in-a-sphere envelope function approach as described previously.[61] The potential for both electrons and holes was assumed to step up by 4 eV at the edge of the NC, defined as the distance from the origin of the most distant atom. The electron and hole effective masses were taken to be 0.11 and 0.42 m_e, respectively. Valence-band mixing, which mixes a small amount of the spatial wave function with angular momentum $\ell + 2$ into the envelope function with nominal angular momentum ℓ, was taken into account for the $1S_{3/2}$ and $2S_{3/2}$ hole states as described in ref 61. The 1P states were treated as pure $\ell = 1$ envelope functions because of the greater complexity involved in including the valence-band mixing[62] (see Discussion). Once the wave functions were calculated, the changes in charge distribution produced by electron–hole pair formation were calculated by assigning each Cd (Se) atom a charge equal to the square of the electron (hole) wave function at that point in space, normalizing the total charge to unity. The Huang–Rhys factor for each phonon mode i is given by $S_i = \Delta_i^2/2$, where Δ_i, the displacement between ground and excited electronic state minima along dimensionless coordinate i in the linear electron–phonon coupling limit, is given by $dE_{eg}/dq_i = \hbar\omega_i\Delta_i$, where E_{eg} is the energy difference between excited and ground states. E_{eg} was calculated as the difference between the Coulombic energy when the atoms have their ground-state charges (taken as the Rabani charges of ±1.18) and that when the atomic charges have been modified by electron–hole pair formation.[61] This purely Coulombic mechanism of electron–phonon coupling is perhaps inconsistent with the purely covalent Tersoff potential (the band gap transition is nominally a Se 4P–Cd 5S transition). However, for the ground-state structure and phonon frequencies, the relative coupling strengths of different phonon modes do not depend on the values assumed for the ground-state charges.

The resonance Raman spectra were calculated by assuming that the Raman intensity in mode i is proportional to $\Delta_i^2\omega_i^2$, the slope of the excited-state potential energy surface along the ground-state dimensionless phonon coordinate, and assigning a Lorentzian line width of 4 cm^{-1} (fwhm) to each phonon transition. $I \sim \Delta^2\omega^2$ is usually a good approximation for low-frequency vibrations and unstructured electronic spectra. Only the Raman fundamentals were calculated.

In order to determine the influence of surface atoms on the phonon modes at different frequencies, the Raman intensities were calculated using two different assumptions about the extent of the electron and hole wave functions: either their effective radius is equal to the actual radius of the nanostructure, or their effective radius is 75% of this value. In the latter case, an artificial assumption that is not intended to represent physical reality, the wave functions do not extend to the surface of the nanocrystal and motions of surface atoms do not contribute to the Huang–Rhys factors, so any surface-localized modes will make a very small contribution to the calculated Raman spectrum.

Conflict of Interest: The authors declare no competing financial interest.

Acknowledgment. This work was supported by NSF Grant No. CHE-1112192.

Supporting Information Available: Resonance Raman spectra extended into the optical phonon overtone region for the samples shown in Figure 2. This material is available free of charge *via* the Internet at http://pubs.acs.org.

REFERENCES AND NOTES

1. Hermann, C.; Yu, P. Y. Role of Elastic Exciton-Defect Scattering in Resonant Raman and Resonant Brillouin Scattering in CdSe. *Phys. Rev. B* **1980**, *21*, 3675–3688.
2. Gross, E.; Permogorov, S.; Morozenko, Y.; Kharlamov, B. Hot-Exciton Luminescence in CdSe Crystals. *Phys. Status Solidi B* **1973**, *59*, 551–560.
3. Yu, P. Y.; Smith, J. E., Jr. Transformation from Raman Scattering to Photoluminescence at the C Exciton of CdSe. *Phys. Rev. Lett.* **1976**, *37*, 622–625.
4. Alivisatos, A. P.; Harris, T. D.; Carroll, P. J.; Steigerwald, M. L.; Brus, L. E. Electron-Vibration Coupling in Semiconductor Clusters Studied by Resonance Raman Spectroscopy. *J. Chem. Phys.* **1989**, *90*, 3463–3468.
5. Klein, M. C.; Hache, F.; Ricard, D.; Flytzanis, C. Size Dependence of Electron–Phonon Coupling in Semiconductor Nanospheres: The Case of CdSe. *Phys. Rev. B* **1990**, *42*, 11123–11132.
6. Baranov, A. V.; Rakovich, Y. P.; Donegan, J. F.; Perova, T. S.; Moore, R. A.; Talapin, D. V.; Rogach, A. L.; Masumoto, Y.; Nabiev, I. Effect of ZnS Shell Thickness on the Phonon Spectra in CdSe Quantum Dots. *Phys. Rev. B* **2003**, *68*, 165306.
7. Dzhagan, V. M.; Valakh, M. Y.; Raevska, O. E.; Stroyuk, O. L.; Kuchmiy, S. Y.; Zahn, D. R. T. The Influence of Shell Parameters on Phonons in Core–Shell Nanoparticles: A Resonant Raman Study. *Nanotechnology* **2009**, *20*, 365704.
8. Kusch, P.; Lange, H.; Artemyev, M.; Thomsen, C. Size-Dependence of the Anharmonicities in the Vibrational Potential of Colloidal CdSe Nanocrystals. *Solid State Commun.* **2011**, *151*, 67–70.
9. Rolo, A. G.; Vasilevskiy, M. I. Raman Spectroscopy of Optical Phonons Confined in Semiconductor Quantum Dots and Nanocrystals. *J. Raman Spectrosc.* **2007**, *38*, 618–633.
10. Kelley, A. M.; Dai, Q.; Jiang, Z.-j.; Baker, J. A.; Kelley, D. F. Resonance Raman Spectra of Wurtzite and Zincblende CdSe Nanocrystals. *Chem. Phys.* **2013**, *422*, 272–276.
11. Baker, J. A.; Kelley, D. F.; Kelley, A. M. Resonance Raman and Photoluminescence Excitation Profiles and Excited-State Dynamics in CdSe Nanocrystals. *J. Chem. Phys.* **2013**, *139*, 024702.
12. Chilla, G.; Kipp, T.; Menke, T.; Heitmann, D.; Nikolic, M.; Fromsdorf, A.; Kornowski, A.; Forster, S.; Weller, H. Direct Observation of Confined Acoustic Phonons in the Photoluminescence Spectra of a Single CdSe–CdS–ZnS Core–Shell–Shell Nanocrystal. *Phys. Rev. Lett.* **2008**, *100*, 057403.
13. Fernée, M. J.; Littleton, B. N.; Cooper, S.; Rubinsztein-Dunlop, H.; Gomez, D. E.; Mulvaney, P. Acoustic Phonon Contributions to the Emission Spectrum of Single CdSe Nanocrystals. *J. Phys. Chem. C* **2008**, *112*, 1878–1884.
14. Fernée, M. J.; Tamarat, P.; Lounis, B. Cryogenic Single-Nanocrystal Spectroscopy: Reading the Spectral Fingerprint of Individual CdSe Quantum Dots. *J. Phys. Chem. Lett.* **2013**, *4*, 609–618.
15. Norris, D. J.; Efros, A. L.; Rosen, M.; Bawendi, M. G. Size Dependence of Exciton Fine Structure in CdSe Quantum Dots. *Phys. Rev. B* **1996**, *53*, 16347–16354.
16. Empedocles, S. A.; Norris, D. J.; Bawendi, M. G. Photoluminescence Spectroscopy of Single CdSe Nanocrystallite Quantum Dots. *Phys. Rev. Lett.* **1996**, *77*, 3873–3876.
17. Groeneveld, E.; de Mello Donegá, C. Enhanced Exciton–Phonon Coupling in Colloidal Type-II CdTe–CdSe Heteronanocrystals. *J. Phys. Chem. C* **2012**, *116*, 16240–16250.
18. Sagar, D. M.; Cooney, R. R.; Sewall, S. L.; Dias, E. A.; Barsan, M. M.; Butler, I. S.; Kambhampati, P. Size Dependent, State-Resolved Studies of Exciton–Phonon Couplings in Strongly Confined Semiconductor Quantum Dots. *Phys. Rev. B* **2008**, *77*, 235321.

19. Sagar, D. M.; Cooney, R. R.; Sewall, S. L.; Kambhampati, P. State-Resolved Exciton−Phonon Couplings in CdSe Semiconductor Quantum Dots. *J. Phys. Chem. C* **2008**, *112*, 9124–9127.
20. Mittleman, D. M.; Schoenlein, R. W.; Shiang, J. J.; Colvin, V. L.; Alivisatos, A. P.; Shank, C. V. Quantum Size Dependence of Femtosecond Electronic Dephasing and Vibrational Dynamics in CdSe Nanocrystals. *Phys. Rev. B* **1994**, *49*, 14435–14447.
21. Salvador, M. R.; Graham, M. W.; Scholes, G. D. Exciton−Phonon Coupling and Disorder in the Excited States of CdSe Colloidal Quantum Dots. *J. Chem. Phys.* **2006**, *125*, 184709.
22. Salvador, M. R.; Hines, M. A.; Scholes, G. D. Exciton−Bath Coupling and Inhomogeneous Broadening in the Optical Spectroscopy of Semiconductor Quantum Dots. *J. Chem. Phys.* **2003**, *118*, 9380–9387.
23. McKimmie, L. J.; Lincoln, C. N.; Jasieniak, J.; Smith, T. A. Three-Pulse Photon Echo Peak Shift Measurements of Capped CdSe Quantum Dots. *J. Phys. Chem. C* **2010**, *114*, 82–88.
24. Roy, A.; Sood, A. K. Surface and Confined Optical Phonons in CdS_xSe_{1-x} Nanoparticles in a Glass Matrix. *Phys. Rev. B* **1996**, *53*, 12127–12132.
25. Krahne, R.; Chilla, G.; Schuller, C.; Carbone, L.; Kudera, S.; Mannarini, G.; Manna, L.; Heitmann, D.; Cingolani, R. Confinement Effects on Optical Phonons in Polar Tetrapod Nanocrystals Detected by Resonant Inelastic Light Scattering. *Nano Lett.* **2006**, *6*, 478–482.
26. Todescato, F.; Minotto, A.; Signorini, R.; Jasieniak, J. J.; Bozio, R. Investigation into the Heterostructure Interface of CdSe-Based Core−Shell Quantum Dots Using Surface-Enhanced Raman Spectroscopy. *ACS Nano* **2013**, *7*, 6649–6657.
27. Tschirner, N.; Lange, H.; Schliwa, A.; Biermann, A.; Thomsen, C.; Lambert, K.; Gomes, R.; Hens, Z. Interfacial Alloying in CdSe/CdS Heteronanocrystals: A Raman Spectroscopy Analysis. *Chem. Mater.* **2012**, *24*, 311–318.
28. Lange, H.; Machon, M.; Artemyev, M.; Woggon, U.; Thomsen, C. Effect of ZnS Shell on the Raman Spectra from CdSe Nanorods. *Phys. Status Solidi RRL* **2007**, *1*, 274–276.
29. Lange, H.; Artemyev, M.; Woggon, U.; Thomsen, C. Geometry Dependence of the Phonon Modes in CdSe Nanorods. *Nanotechnology* **2009**, *20*, 045705.
30. Dzhagan, V. M.; Lokteva, I.; Himcinschi, C.; Kolny-Olesiak, J.; Valakh, M. Y.; Schulze, S.; Zahn, D. R. T. The Influence of Pyridine Ligand onto the Structure and Phonon Spectra of CdSe Nanocrystals. *J. Appl. Phys.* **2011**, *109*, 084334.
31. Giugni, A.; Das, G.; Alabastri, A.; Zaccaria, R. P.; Zanella, M.; Franchini, I.; Di Fabrizio, E.; Krahne, R. Optical Phonon Modes in Ordered Core−Shell CdSe/CdS Nanorod Arrays. *Phys. Rev. B* **2012**, *85*, 115413.
32. Nobile, C.; Fonoberov, V. A.; Kudera, S.; Della Torre, A.; Ruffino, A.; Chilla, G.; Kipp, T.; Heitmann, D.; Manna, L.; Cingolani, R.; *et al.* Confined Optical Phonon Modes in Aligned Nanorod Arrays Detected by Resonant Inelastic Light Scattering. *Nano Lett.* **2007**, *7*, 476–479.
33. Lu, L.; Xu, X.-L.; Liang, W.-T.; Lu, H.-F. Raman Analysis of CdSe/CdS Core−Shell Quantum Dots with Different CdS Shell Thickness. *J. Phys.: Condens. Matter* **2007**, *19*, 406221.
34. Hwang, Y.-N.; Park, S.-H.; Kim, D. Size-Dependent Surface Phonon Mode of CdSe Quantum Dots. *Phys. Rev. B* **1999**, *59*, 7285–7288.
35. Cherevkov, S. A.; Fedorov, A. V.; Artemyev, M. V.; Prudnikau, A. V.; Baranov, A. V. Anisotropy of Electron−Phonon Interaction in Nanoscale CdSe Platelets As Seen *via* Off-Resonant and Resonant Raman Spectroscopy. *Phys. Rev. B* **2013**, *88*, 041303.
36. Venugopal, R.; Lin, P.-I.; Liu, C.-C.; Chen, Y.-T. Surface-Enhanced Raman Scattering and Polarized Photoluminescence from Catalytically Grown CdSe Nanobelts and Sheets. *J. Am. Chem. Soc.* **2005**, *127*, 11262–11268.
37. Ruppin, R.; Englman, R. Optical Phonons of Small Crystals. *Rep. Prog. Phys.* **1970**, *33*, 149–196.
38. Fonoberov, V. A.; Balandin, A. A. Interface and Confined Optical Phonons in Wurtzite Nanocrystals. *Phys. Rev. B* **2004**, *70*, 233205.
39. Trallero-Giner, C.; Debernardi, A.; Cardona, M.; Menendez-Proupin, E.; Ekimov, A. I. Optical Vibrons in CdSe Dots and Dispersion Relation of the Bulk Material. *Phys. Rev. B* **1998**, *57*, 4664–4669.
40. Cirillo, M.; Aubert, T.; Gomes, R.; Van Deun, R.; Emplit, P.; Biermann, A.; Lange, H.; Thomsen, C.; Brainis, E.; Hens, Z. "Flash" Synthesis of CdSe/CdS Core−Shell Quantum Dots. *Chem. Mater.* **2014**, *26*, 1154–1160.
41. Norris, D. J.; Bawendi, M. G. Measurement and Assignment of the Size-Dependent Optical Spectrum in CdSe Quantum Dots. *Phys. Rev. B* **1996**, *53*, 16338–16346.
42. Rabani, E. An Interatomic Pair Potential for Cadmium Selenide. *J. Chem. Phys.* **2002**, *116*, 258–262.
43. Benkabou, F.; Aourag, H.; Certier, M. Atomistic Study of Zinc-Blende CdS, CdSe, ZnS, and ZnSe from Molecular Dynamics. *Mater. Chem. Phys.* **2000**, *66*, 10–16.
44. Widulle, F.; Kramp, S.; Pyka, N. M.; Gobel, A.; Ruf, T.; Debernardi, A.; Lauck, R.; Cardona, M. The Phonon Dispersion of Wurtzite CdSe. *Physica B* **1999**, *263−264*, 448–451.
45. Yu, P. Y.; Cardona, M. *Fundamentals of Semiconductors*, 3rd ed.; Springer-Verlag: Berlin, 2001.
46. Singh, J. *Physics of Semiconductors and Their Heterostructures*; McGraw-Hill Education: New York, 1993.
47. Talapin, D. V.; Nelson, J. H.; Shevchenko, E. V.; Aloni, S.; Sadtler, B.; Alivisatos, A. P. Seeded Growth of Highly Luminescent CdSe/CdS Nanoheterostructures with Rod and Tetrapod Morphologies. *Nano Lett.* **2007**, *7*, 2951–2959.
48. Ren, S.-F.; Cheng, W.; Yu, P. Y. Microscopic Investigation of Phonon Modes in SiGe Alloy Nanocrystals. *Phys. Rev. B* **2004**, *69*, 235327.
49. Ren, S.-F.; Lu, D.; Qin, G. Phonon Modes in InAs Quantum Dots. *Phys. Rev. B* **2001**, *63*, 195315.
50. Khoo, K. H.; Zayak, A. T.; Kwak, H.; Chelikowsky, J. R. First-Principles Study of Confinement Effects on the Raman Spectra of Si Nanocrystals. *Phys. Rev. Lett.* **2010**, *105*, 115504.
51. Cheng, W.; Ren, S.-F.; Yu, P. Y. Theoretical Investigation of the Surface Vibrational Modes in Germanium Nanocrystals. *Phys. Rev. B* **2003**, *68*, 193309.
52. Fu, H.; Ozolins, V.; Zunger, A. Phonons in GaP Quantum Dots. *Phys. Rev. B* **1999**, *59*, 2881–2887.
53. Han, P.; Bester, G. Confinement Effects on the Vibrational Properties of III−V and II−VI Nanoclusters. *Phys. Rev. B* **2012**, *85*, 041306(R).
54. Cai, X. C.; Martin, J. E.; Shea-Rohwer, L. E.; Gong, K.; Kelley, D. F. Thermal Quenching Mechanisms in II−VI Semiconductor Nanocrystals. *J. Phys. Chem. C* **2013**, *117*, 7902–7913.
55. Gong, K.; Zeng, Y. H.; Kelley, D. F. Extinction Coefficients, Oscillator Strengths, and Radiative Lifetimes of CdSe, CdTe, and CdTe/CdSe Nanocrystals. *J. Phys. Chem. C* **2013**, *117*, 20268–20279.
56. Capek, R. K.; Moreels, I.; Lambert, K.; De Muynck, D.; Zhao, Q.; Van Tomme, A.; Vanhaecke, F.; Hens, Z. Optical Properties of Zincblende Cadmium Selenide Quantum Dots. *J. Phys. Chem. C* **2010**, *114*, 6371–6376.
57. Mohamed, M. B.; Tonti, D.; Al-Salman, A.; Chemseddine, A.; Chergui, M. Synthesis of High Quality Zinc Blende CdSe Nanocrystals. *J. Phys. Chem. B* **2005**, *109*, 10533–10537.
58. Mahler, B.; Lequeux, N.; Dubertret, B. Ligand-Controlled Polytypism of Thick-Shell CdSe/CdS Nanocrystals. *J. Am. Chem. Soc.* **2010**, *132*, 953–959.
59. Nan, W.; Niu, Y.; Qin, H.; Cui, F.; Yang, Y.; Lai, R.; Lin, W.; Peng, X. Crystal Structure Control of Zinc-Blende CdSe/CdS Core/Shell Nanocrystals: Synthesis and Structure-Dependent Optical Properties. *J. Am. Chem. Soc.* **2012**, *134*, 19685–19693.
60. Gale, J. D.; Rohl, A. L. The General Utility Lattice Program (GULP). *Mol. Simul.* **2003**, *29*, 291–341.
61. Kelley, A. M. Electron−Phonon Coupling in CdSe Nanocrystals from an Atomistic Phonon Model. *ACS Nano* **2011**, *5*, 5254–5262.
62. Ekimov, A. I.; Hache, F.; Schanne-Klein, M. C.; Ricard, D.; Flytzanis, C.; Kudryavtsev, I. A.; Yazeva, T. V.; Rodina, A. V. Absorption and Intensity-Dependent Photoluminescence Measurements on CdSe Quantum Dots: Assignment of the First Electronic Transition. *J. Opt. Soc. Am. B* **1993**, *10*, 100–107.